



MoS 2 -Polyaniline Based Flexible Electrochemical Biosensor: Toward pH Monitoring in Human Sweat

Choudhury, S., Deepak, D., Bhattacharya, G., McLaughlin, J., & Roy, S. S. (2023). MoS 2 -Polyaniline Based Flexible Electrochemical Biosensor: Toward pH Monitoring in Human Sweat. *Macromolecular Materials and Engineering*, 1-12. [2300007]. <https://doi.org/10.1002/mame.202300007>

[Link to publication record in Ulster University Research Portal](#)

Published in:
Macromolecular Materials and Engineering

Publication Status:
Published online: 17/04/2023

DOI:
[10.1002/mame.202300007](https://doi.org/10.1002/mame.202300007)

Document Version
Publisher's PDF, also known as Version of record

General rights
Copyright for the publications made accessible via Ulster University's Research Portal is retained by the author(s) and / or other copyright owners and it is a condition of accessing these publications that users recognise and abide by the legal requirements associated with these rights.

Take down policy
The Research Portal is Ulster University's institutional repository that provides access to Ulster's research outputs. Every effort has been made to ensure that content in the Research Portal does not infringe any person's rights, or applicable UK laws. If you discover content in the Research Portal that you believe breaches copyright or violates any law, please contact pure-support@ulster.ac.uk.

MoS₂-Polyaniline Based Flexible Electrochemical Biosensor: Toward pH Monitoring in Human Sweat

Sudipta Choudhury, Deepak Deepak, Gourav Bhattacharya, James McLaughlin, and Susanta Sinha Roy*

Wearable pH sensors for sweat analysis have garnered significant scientific attention for the detection of early signs of many physiological diseases. In this study, a MoS₂-polyaniline (PANI) modified screen-printed carbon electrode (SPCE) is fabricated and used as a sweat biosensor. The exfoliated MoS₂ nanosheets are drop casted over an SPCE and are functionalized by a conducting polymer, polyaniline (PANI) via the electropolymerization technique. The as-fabricated biosensor exhibits high super-Nernstian sensitivity of -70.4 ± 1.7 mV pH⁻¹ in the linear range of pH 4 to 8 of 0.1 M standard phosphate buffer solution (PBS), with outstanding reproducibility. The sensor exhibits excellent selectivity against the common sweat ions including Na⁺, Cl⁻, K⁺, and NH₄⁺ with tremendous long-term stability over 180 min from pH 4 to 6. The enhanced active surface area and better electrical conductivity as a consequence of the synergistic effect between MoS₂ and PANI are correlated with the boosted performance of the as-produced biosensor. The feasibility of the sensor is further examined using an artificial sweat specimen and the successful detection confirms the potential of the biosensor for a real-time noninvasive, skin attachable, and flexible wearable pH sensor.

popular method for analyzing and continuous real-time monitoring of human body fluids such as urine, blood, sweat, tears, saliva, and interstitial fluid (IF).^[1–6] Recent advancement in wearable sensors, in particular, electrochemical sensors has drawn tremendous attention because of their relatively high sensitivity, selectivity, fast response time, good compatibility, and ease of measurement.^[3,7,8] An individual's health and physical condition can be assessed by detecting and quantifying the concentrations of biomarkers such as electrolytes, metabolites, proteins, peptides, antibodies, ions, and hormones.^[9–12] Detecting biomarkers conventionally, which generally requires blood or IF samples is costly, invasive, and time consuming.^[13] In contrast, sweat has shown great promise for wearable sensing as it can be monitored noninvasively and continuously at a low cost.^[14] Human sweat is an important biological fluid which provides a wealth of information about the health and fitness


1. Introduction

With the rapid growth of interest in healthcare technologies over the past decades, wearable biosensors have become a

status of a person at a molecular level.^[1,15] Sweat is secreted from eccrine sweat glands which contain primarily water (98–99%) and also a treasure trove of biomarkers including ions (Na⁺, K⁺, H⁺, Ca²⁺, NH₄⁺, Cl⁻ etc.), pH, small molecules such as glucose, lactate, urea, cortisol, uric acid, urea and small proteins, and peptides.^[16,17]

Among various sensors, pH sensors are most significant in a variety of sectors including biological, chemical, materials, and environmental studies as well as the food industry, healthcare monitoring, and disease diagnostics.^[2,6,18–21] pH is a significant health indicator as it displays the equilibrium level of electrolytes and metabolic activity through the hydrogen ion concentration in body fluids, thus providing rich information about the physiological condition of a person.^[22–24] For instance, patients with cystic fibrosis are reported to have alkaline sweat (up to pH 9) as compared to a healthy person (4.5–6.5), due to the defect in bicarbonate reabsorption.^[25] Furthermore, kidney stones in type II diabetic patients are reported to have lower sweat pH than a normal person.^[26] Skin illnesses such as acne vulgaris, ichthyosis, and candida albicans infections are also affected by pH.^[27,28] In addition, the pH value of normal skin shows slightly acidic (pH 5.5) but in the case of chronic wounds pH values often exhibit greater than 7.4 due to the presence of bacterial colonies and enzymes.^[29] Sweat pH also provides crucial information on

S. Choudhury, D. Deepak, S. S. Roy
 Department of Physics
 School of Natural Sciences
 Shiv Nadar (Institute of Eminence Deemed to be University)
 Gautam Buddha Nagar, Uttar Pradesh 201314, India
 E-mail: susanta.roy@snu.edu.in
 G. Bhattacharya, J. McLaughlin
 Nanotechnology and Integrated Bioengineering Centre
 School of Engineering
 Ulster University
 Newtownabbey, Belfast, Northern Ireland BT37 0QB, UK

 The ORCID identification number(s) for the author(s) of this article can be found under <https://doi.org/10.1002/mame.202300007>

© 2023 The Authors. Macromolecular Materials and Engineering published by Wiley-VCH GmbH. This is an open access article under the terms of the Creative Commons Attribution License, which permits use, distribution and reproduction in any medium, provided the original work is properly cited.

DOI: 10.1002/mame.202300007

sweat rate, dehydration level, and epidermal physiological health. Therefore, accurate and reliable measurement of pH in sweat is required for the diagnosis of specific health problems. Conventional liquid-junction glass pH electrodes are not relevant for wearable bioelectronics due to a few inherent drawbacks including high-temperature instability, acid and alkaline errors, and lack of flexibility or bending capability which hinder their applications in these fields.^[30,31]

Mostly used pH sensor devices are based on potentiometric electrodes, conductimetric/chemiresistors or ion-selective field effect transistors (ISFET), or chemoresistor transistors^[21,32–34] fabricated on various substrates such as polyimide (PI), polyethylene terephthalate (PET), parylene, or polyethylene naphthalene (PEN). In comparison to other analytical tools, potentiometric measurements are favored due to their high sensitivity, wide sensing range, fast response, less interference, low power and long lifetime, and ease of use in wireless systems.^[2,35] Advanced flexible potentiometric pH sensors include polymer-based pH sensors, microfabricated electrochemical pH sensors, and MO_x -based sensors.^[30,34,36] Several organic conducting polymers and their composites such as PEDOT:PSS, polyaniline/polyurethane, gold/polyaniline, and graphite-polyurethane provide excellent pH sensing performance because of their superior electrochemical properties comprising the variation in oxidation states and ion-exchange.^[36,37]

During the past several years, polyaniline (PANI) has been used as conducting polymer electrodes, and devices to create lightweight and flexible electronics because of its superior flexibility and lower density in comparison with other metal oxides. However, the low practical capacitance and poor cycling stability seriously limit their applications as promising electrode materials. Significant efforts to improve the overall performance of PANI-based electrochemical sensors are being made via surface modifications, etching, and hybrid nanostructures. PANI has also garnered much attention for sensing H^+ ions through protonation-deprotonation on the electrode surface. It can selectively bind only H^+ ions from the pH solutions mixed with other ions and metabolites. Among all such alterations, PANI hybrid with 2D layered materials has been proven to be excellent and garnered tremendous attention in the biosensing technology due to increased performance rate.^[38–40] Currently, among all 2D transition metal dichalcogenides (TMDs), such as molybdenum disulfide (MoS_2) have attained exuberant attention among researchers in the area of electrochemical biosensors due to large surface area, tunable band gap, high chemical stability, high electron mobility, excellent electrocatalytic properties, and ion-intercalation surface morphologies.^[41–43] The graphene-like structure of MoS_2 possesses a high surface-to-volume ratio and its superior layer spacing (0.65 nm) than graphene (0.34 nm) facilitates the probability of insertion of a large number of biospecies.^[40] However, restacking between layers due to van der Waals forces limits its application for electrochemical sensing.^[44] Therefore, functionalization with other materials may improve their performances as electrochemical sensor. The surface functionalization with conductive polymer will be a good approach to enhance the electrochemical properties and cyclic stability. A few reports have been published regarding few-layer MoS_2 with PANI nanocomposites as biosensors^[43–45] showing that

these architectures hold immense potential for next-generation healthcare monitoring platforms.

In this present work, we report on the fabrication of an inexpensive and flexible MoS_2 -PANI modified screen-printed carbon electrode as an electrochemical pH sensor. The modified electrodes were tested using different buffer solutions from pH 4 to 8 using the open circuit potential (OCP) method. The hybrid MoS_2 -PANI/SPCE electrodes showed higher electrochemical active surface area (ECSA), and high specific capacitance which significantly improve ion-to-electron transduction. The electrochemical pH sensor also featured excellent sensitivity, reproducibility, and high selectivity against other possibly interfering ions and organic molecules. Finally, the sensor's response toward artificial sweat was also investigated and it showed good Nernstian response and stability of the sensor. This proposed sensor indicates the high potential of its application in wearable devices for real-time continuous monitoring of pH in human sweat.

2. Experimental Section

2.1. Materials and Methodology

2.1.1. Material Characterization

The surface morphology and elemental composition of the samples were investigated by using field emission scanning electron microscopy (FE-SEM) (JEOL JSM-7610F Plus) and energy dispersive X-ray spectroscopy (EDS) (EDAX AMETEK). X-ray diffraction (XRD) spectra of nanocomposites were carried out using Bruker D8-Discover with $\text{Cu-K}\alpha$ radiation ($\lambda = 1.5406 \text{ \AA}$) using a Lynx Eye detector. UV-Vis-NIR spectrophotometer (Shimadzu, Solidspec 3700) was used to measure the absorbance of MoS_2 nanosheets in the wavelength range of 300–800 nm applying an unpolarized light. Raman spectroscopy was conducted by using a micro-Raman spectrometer (STR) equipped with a 532 nm argon-ion laser source with a power of 2.5 mW and 50 \times magnification objective lens. Photoluminescence spectra were obtained with Fluoromax 4C Horiba Scientific spectrofluorometer upon excitation of a series of wavelengths using 450 W Xenon lamp. Transmission electron microscopy (TEM) images, high-resolution transmission electron microscopy (HRTEM), and selected area electron diffraction (SAED) of the MoS_2 nanosheets and MoS_2 -PANI composite were captured at 200 kV on a JEOL JEM-F200 TEM. X-ray photoelectron spectroscopy (XPS) spectra were acquired with a ThermoFisher ESCALAB XI instrument. A monochromated Al (operated at a voltage of 15 kV with a current of 15 mA and a power of 225 W) was used as the excitation source. A flood gun was used for charge compensation purposes.

2.1.2. Chemicals and Materials

Potassium phosphate monobasic (KH_2PO_4), potassium phosphate dibasic (K_2HPO_4), hydrochloric acid (HCl), KOH, NaCl, KNO_3 , NH_4Cl , lactic acid, uric acid, aniline, bulk MoS_2 , and DMF were purchased from Sigma Aldrich (India). All the chemicals were analytical grade and used without any purification process. Phosphate buffer solutions (PBS 0.1 M) with various pH values

(from 4 to 9) were prepared with different amounts of KH_2PO_4 and K_2HPO_4 and adjusted with 1 M HCl or 1 M KOH solutions. Artificial sweat containing 0.45×10^{-3} M NH_4Cl , 1.75×10^{-3} M KNO_3 , 25×10^{-3} M NaCl, 25×10^{-6} M uric acid, and 7.5×10^{-3} M lactic acid with varying pH was used. The aqueous solution was prepared by using pure deionized water (resistivity 18.2 M Ω cm). Screen-printed carbon electrodes were purchased from Sinsil International Pvt. Ltd. (India).

2.1.3. Synthesis of Exfoliated MoS_2 and PANI Functionalized Electrodes (MoS_2 -PANI/SPCE)

2D MoS_2 nanosheets were synthesized by the liquid-phase exfoliation (LPE) method in an organic solvent. To obtain nanosheets, 100 mg of bulk MoS_2 powder was ground for 30 min in a mortar pestle with periodic addition of a small amount of DMF. Obtained MoS_2 paste was transferred to a beaker which contains 20 mL DMF. Thus, MoS_2 concentration in DMF was calculated to be 5 mg mL $^{-1}$. This solution was magnetically stirred at 600 rpm to obtain a homogenous mixture. Thereafter, it is left for ultrasonication for 24 h in a bath sonicator. The obtained solution is centrifuged at 2500 rpm and supernatants were collected in centrifuge tubes which refers to MoS_2 nanosheets.

After exfoliation of MoS_2 nanosheets in DMF solvent, 10 μL of the stock solution was drop-casted on the SPCE and dried in an oven at 60 $^\circ\text{C}$ for 10 min for complete removal of solvent which is essential for coating of MoS_2 on the electrode surface. This SPCE was used as a substrate with the goal of the flexibility of the pH sensors. Then the working electrode for the pH sensor was fabricated by electrodeposition of PANI via a potentiometric technique. The potentiometric deposition technique was carried out for 30 cycles by cyclic voltammetry (CV) at a scan rate of 100 mV s $^{-1}$ in a solution of 0.1 M aniline (in 1 M HCl) from -0.2 to 1.0 V. Also, electropolymerization of PANI onto the MoS_2 -SPCE was optimized using different CV cycles (Figure S2, Supporting Information). Evidence for electropolymerization of aniline on the MoS_2 -SPCE electrode is shown in Figure S1 (Supporting Information), where the area of the CV increases with the increasing number of cycles. After the deposition, the film was gently rinsed with deionized water and dried at 50 $^\circ\text{C}$ for half an hour. Here, Ag/AgCl (3 M KCl) and Pt wire were used as reference and counter electrodes. Finally, a MoS_2 -PANI/SPCE-based pH sensor was fabricated.

2.2. Electrochemical Measurements

CV and measurements of OCPs were carried out using an Autolab potentiostat/galvanostat 302N instrument (Metrohm B.V., Utrecht, Netherlands) controlled by Nova (version 1.10) software. For the CV study, a standard three-electrode setup was used, which included a working electrode (MoS_2 -PANI/SPCE), a Pt wire as a counter electrode, and Ag/AgCl (with 3 M KCl electrolyte) as a reference electrode. To execute the electrochemical measurements, two types of electrolytes were used. At first, an aqueous solution of 1 M Na_2SO_4 for the electric double layer capacitance (EDLC) and then a redox-active electrolyte of 5 mmol L $^{-1}$ $[\text{Fe}(\text{CN})_6]^{3-/4-}$ in 0.1 M KCl was used to study ECSA and electrochemical impedance spectroscopy (EIS). EIS measurements were executed in FRA potential scan mode with the same

electrode-electrolyte arrangement. A sinusoidal signal having a root-mean-square value of 10 mV was applied as a perturbation within the frequency range of 0.1 Hz to 100 kHz. The as-obtained Nyquist plots were fitted using the NOVA (version 1.10) software. OCP measurements were performed in a two-electrode configuration with MoS_2 -PANI/SPCE as the working electrode and an Ag/AgCl reference electrode. Under open-circuit conditions, no external current is flowing into the system, hence there is no need for the third counter electrode. Supercapacitor performance was tested with a three-electrode assembly in 1 M Na_2SO_4 aqueous electrolyte within a potential window ranging from -0.1 to 0.7 V. All the experiments were carried out at room temperature.

3. Results and Discussion

3.1. Structural and Morphological Characterizations of the Modified SPCE Electrodes

The functionalization of PANI on the exfoliated MoS_2 -SPCE electrode was prepared by two-step processes (i) exfoliation of MoS_2 nanosheets from bulk MoS_2 powder by ultrasonication in DMF and (ii) electropolymerization of aniline on the MoS_2 drop-coated SPCE. The surface morphology, nanostructure, and elemental composition of exfoliated MoS_2 nanosheets, PANI, MoS_2 -PANI, and MoS_2 -PANI/SPCE composites were studied by FESEM and EDS. Figure 1a shows the FESEM images of the surface of exfoliated MoS_2 nanosheets. The inset of Figure 1a displays the synthesized wrinkled few-layer sheets of MoS_2 confirming that the DMF solvent separates the stacks of MoS_2 into individual nanosheets. These nanosheets indicate a high specific surface area which can enhance the electrochemical sensor's performance. The TEM image, SAED pattern, and HRTEM image of MoS_2 nanosheets are shown in Figure S7 (Supporting Information). Figure 1b shows the FESEM image of PANI film which was prepared by depositing the suspension of PANI salt in DMF on a silicon substrate and dried in an oven at 60 $^\circ\text{C}$. The FESEM image of the MoS_2 -PANI mixture shown in Figure 1c, indicates many random agglomerations. MoS_2 -PANI/SPCE composite which is shown in Figure 1d reveals fibrous morphology and interfiber fusion covering the surface of the electrode which further indicates successful electropolymerization of PANI and adsorption on the MoS_2 /SPCE.

Figure 2a,b shows the low-magnification TEM image of the MoS_2 /PANI sample. The TEM image reveals the two contrasted regions: the dark region indicates the nanosheets of exfoliated MoS_2 and the lighter region depicts the conducting PANI polymer. From Figure 2b the stacking of the MoS_2 -PANI composite was observed and hence formed a disordered nanostructure. Overall, it suggests the successful incorporation of exfoliated MoS_2 nanosheets into the conducting polymeric matrix PANI.

Raman spectroscopy is an efficient tool to study the lattice vibration of layered materials and also the interaction between 2D materials and polymer composites.^[46] Figure 3a displays the Raman spectra of bulk MoS_2 and exfoliated nanosheets. In the Raman spectra of bulk MoS_2 two well-defined peaks are observed at 377.8 cm $^{-1}$ (E_{2g}^1) and 404.5 cm $^{-1}$ (A_{1g}). E_{2g}^1 peak is associated with the in-plane vibration (opposite vibration of two S atoms with respect to Mo) of Mo-S bonds and A_{1g} peak corresponds to out-of-plane vibrations of only S atoms in the opposite direction.^[47]

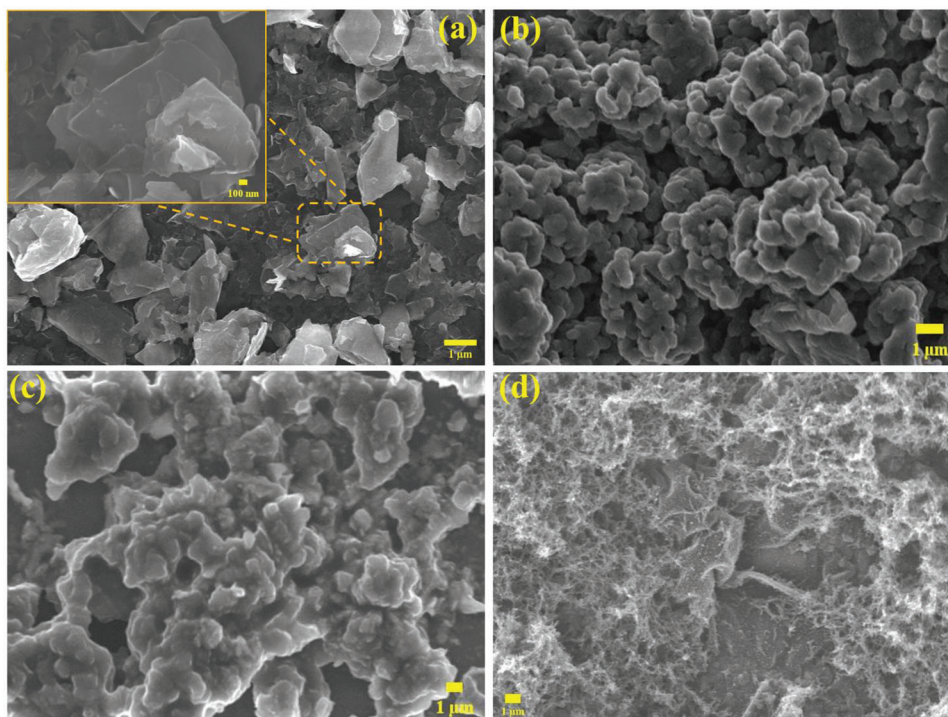


Figure 1. FESEM image of a) exfoliated MoS₂ nanosheets (inset: high magnification), b) PANI, c) MoS₂-PANI mixture, and d) MoS₂-PANI/SPCE composites.

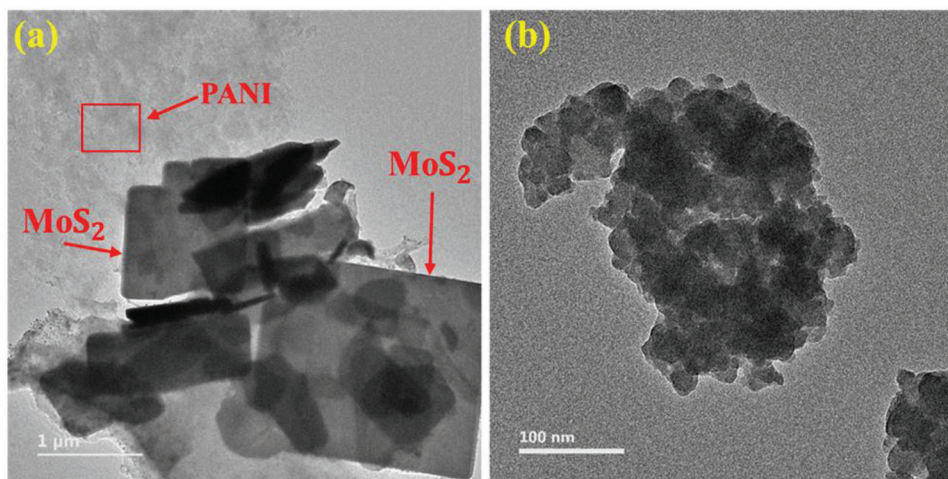


Figure 2. a,b) Transmission electron microscopy (TEM) image of the MoS₂/PANI composite at different magnifications.

However, for exfoliated MoS₂ nanosheets the peaks are shifted to 380.9 cm⁻¹ (E_{2g}^1) and 405.5 cm⁻¹ (A_{1g}) which correspond to the exfoliation that may cause the electron pairs of Mo–S bonds to become more localized, resulting in a shift toward higher energy.^[48] The frequency difference between the two vibrational modes of bulk and exfoliated MoS₂ is 26.7 and 24.6 cm⁻¹, respectively which further confirms the exfoliation of nanosheets.

In the case of bare SPCE, (Figure 3b) prominent D and G (E_{2g}) bands are observed at 1353 and 1579 cm⁻¹, respectively, which are attributed to the edge plane and basal plane sites.^[49]

As seen in Figure 3b, PANI has peaks at 1121 and 1290 cm⁻¹ which correspond to the C–H bending vibrations of benzene and quinoid rings, whereas C=C stretching vibrations of benzenoid and quinoid rings are observed at 1552 cm⁻¹.^[46] Similarly, Raman spectra of MoS₂-SPCE and MoS₂-PANI/SPCE are shown in Figure 3b. No obvious difference is observed in the composite MoS₂-PANI/SPCE electrode compared to PANI and MoS₂-SPCE indicating the effective formation of the hybrid sensor.

The crystal structure of exfoliated MoS₂ and MoS₂-PANI/SPCE composite was characterized by XRD (Figure S7a and Figure 3c).

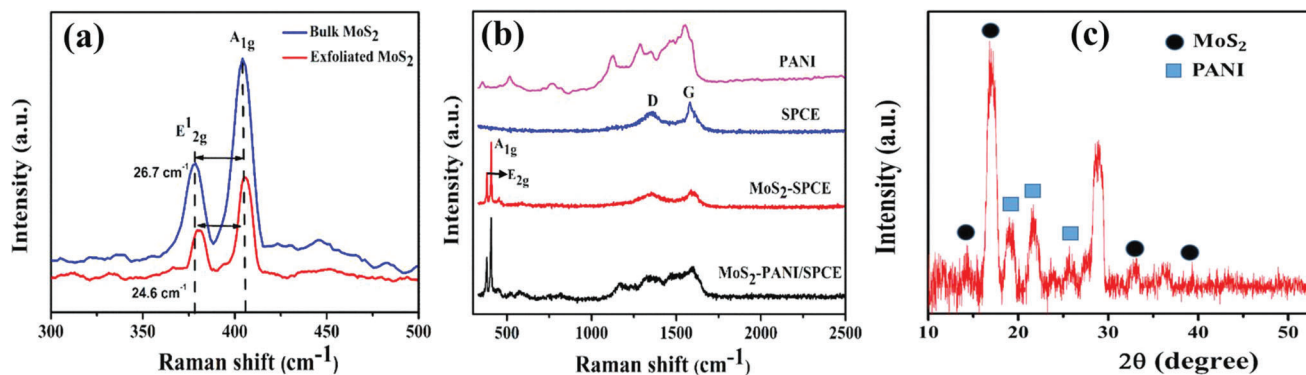


Figure 3. Raman spectra of a) bulk and exfoliated MoS₂, b) PANI, SPCE, MoS₂-SPCE, and MoS₂-PANI/SPCE composites, X-ray diffraction (XRD) pattern of c) MoS₂-PANI/SPCE composites.

In Figure S7a (Supporting Information) the diffraction peaks of exfoliated MoS₂ located at 14.4°, 39.6°, and 49.6° which correspond to the (002), (103), and (105) planes of hexagonal MoS₂ nanosheets after exfoliation.^[48–50] The sharp intense peak at 2θ value 14.4° confirms the nanosheets formation of MoS₂.^[50] In the MoS₂-PANI/SPCE composite (Figure 3c) the diffraction peaks located at 2θ (hkl): 19.1°, 21.7°, and 25.7° which are attributed to the crystalline nature of emeraldine salt form of PANI^[51,52] (marked with blue rectangles) and the peaks (marks with black circles) centered at 14.3°, 17.02°, 32.9° and 39.4° correspond to the (002), (003), (100), (103) planes of MoS₂^[48,53] and the peak at 54.7° occurs because of screen printed carbon substrate. This suggests the deposition and as well as the strong attachment of PANI (ES) on the MoS₂-SPCE substrate. Therefore, PANI deposition by electropolymerization technique does not alter the structural properties of MoS₂ nanosheets.

MoS₂ nanosheets dispersed in DMF were characterized by UV–Vis absorption spectroscopy for further confirmation of exfoliation. Synthesizing 2D MoS₂ nanosheets in an organic solvent by LPE is the most effective method and is compatible with biosensing applications and devices.^[43] The exfoliated MoS₂ nanosheets show four excitonic peaks “A,” “B,” “C,” and “D” in the absorption spectra shown in Figure S7b (Supporting Information). In the case of the bulk form of MoS₂, the valence band maximum is located at the Γ point and the conduction band maximum is located between the Γ and K points which creates an indirect band gap of 1.29 eV.^[43] But with reducing the layer numbers, the conduction band shifts upward which results in a direct band gap transition. The direct band gap of ≈1.87 eV is measured from the Tauc plot which is shown in Figure S7c (Supporting Information). The transition from indirect to the direct band gap of a few layers of MoS₂ can be ascribed to the interlayer interaction, decreasing layer numbers and quantum confinement.^[54]

XPS was further employed to characterize the chemical compositions and to determine the oxidation states of elements present in the MoS₂-PANI composite.^[51] Figure 4a exhibits the XPS survey spectra of the MoS₂-PANI composite and the presence of C, Mo, N, S, and O is confirmed. The small peak of Si 2p can be attributed to the Si substrate where the MoS₂-PANI solution was drop-casted. The deconvoluted XPS spectra of Mo 3d and S 2p are shown in Figure 4b,c. The high-resolution Mo

3d spectrum shows two characteristic peaks at binding energies 229.35 eV (Mo 3d_{5/2}) and 232.4 eV (Mo 3d_{3/2}) which are attributed to Mo (IV) oxidation state.^[55–57] Also, there is a weak peak at binding energy 226.6 eV which can be ascribed to S 2s^[51] Moreover, the other two peaks at binding energies at 235.7 and 232.9 eV correspond to Mo (VI) 3d_{3/2} and Mo (VI) 3d_{5/2}.^[56,57] In the S 2p spectrum (Figure 4c) two intense peaks occur at 163.0 and 161.8 eV which are assigned to S 2p_{1/2} and S 2p_{3/2}, respectively, for the divalent sulphide ions.^[56] The extra deconvoluted peak at binding energy 168.5 eV could be ascribed to the S–C bonds^[58] In the C 1s spectrum (Figure 4d) of the MoS₂-PANI composite a strong peak occurs at binding energy 284.8 eV which can be assigned to C=C/C–C bonds.^[56] In addition, the C–O and COOH/C=O groups are present in the C 1s spectra indicating the presence of oxygen functionalities. The deconvoluted N 1s spectra in Figure 4e consist of four peaks at 395.7, 399, 399.8, and 401.4 eV which can be ascribed to Mo 3p, pyridinic N, pyrrolic N, and Mo–N.^[56,59] As shown in Figure 4f, the O 1s spectra consist of Mo–O and C=O groups at 531.7 and 532.4 eV.^[60] The XPS spectra indicate the formation of the MoS₂-PANI composite and the presence of C–S, and Mo–O chemical bonding confirms the successful electropolymerization process.

For better understanding, XPS spectra of as synthesized MoS₂-PANI/SPCE were compared against other conventional methods of fabrication showing similarities and dissimilarities. For example, Maity et al.^[48] synthesized MoS₂@PANI composites via in situ polymerization and confirmed their synthesis via XPS study. All inherent peaks of PANI in N1s spectra were present, but surprisingly there was no direct evidence of Mo–N peak which is unlikely a case in electrochemical polymerization (our method). Moreover, presence of Mo–N peak in electro polymerization (our method) indicates toward a strong bond formation and better composite nature of MoS₂@PANI over in situ polymerization. In another report, Chen et al.^[61] fabricated MoS₂/PANI@CNT composites via different strategy of mixing MoS₂ and polyaniline separately. N1s spectra of such composite inhibits all four peaks which matches well with the one reported in Figure 4e. In another method, Xuan Li et al.^[59] reported successful synthesis of MoS₂-rGO@PANI via in situ polymerization. XPS spectra of as fabricated composite fits well with our method indicating all three peaks of PANI and strong Mo–N bond at 401.4 eV.

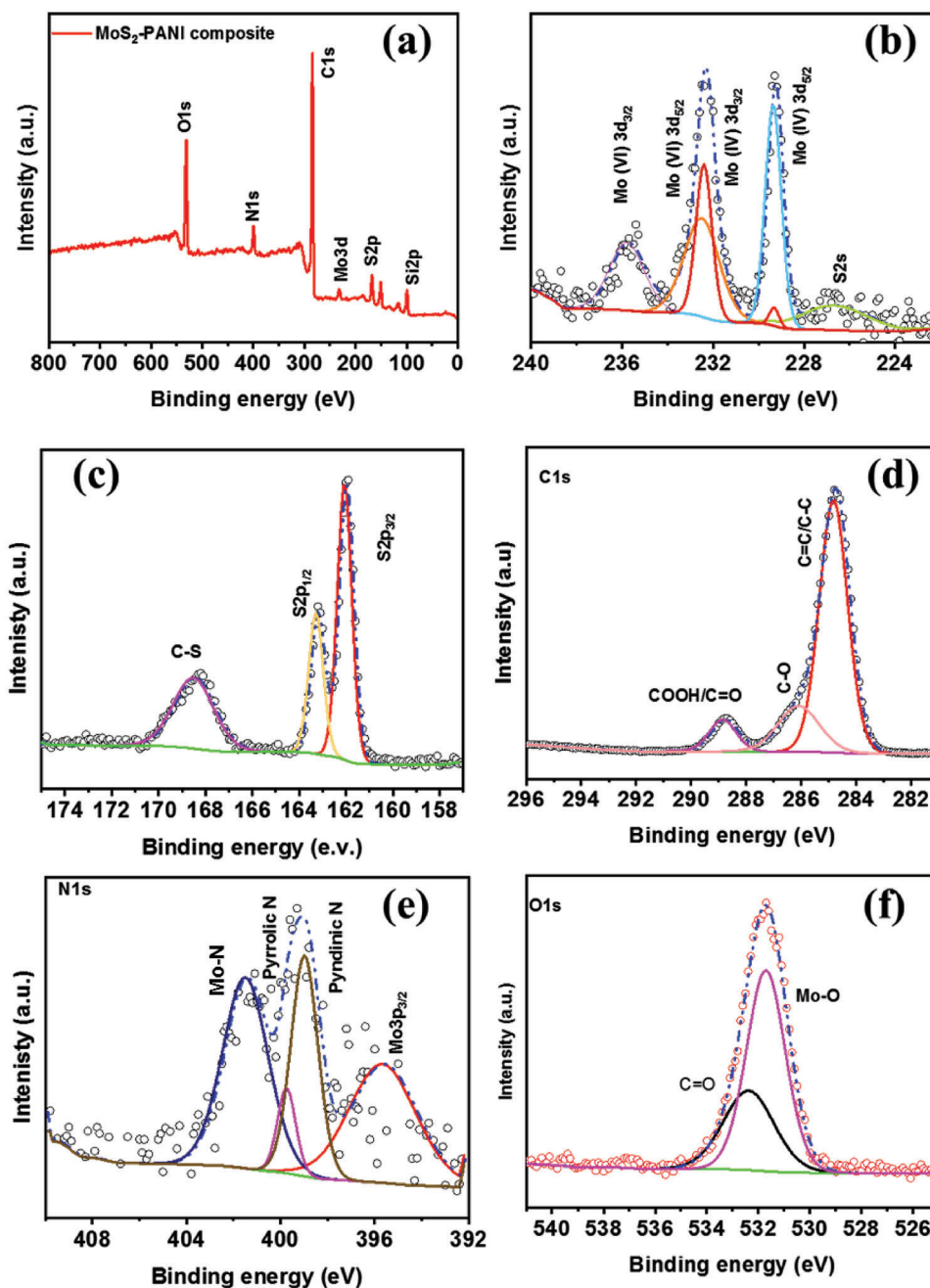


Figure 4. X-ray photoelectron spectroscopy (XPS) spectra for the MoS₂-PANI composite material: a) survey spectrum and high-resolution b) Mo 3d, c) S 2p, d) C 1s, e) N 1s, and f) O 1s spectra.

3.2. Electrochemical Characterization of the Modified Electrodes

The cyclic voltammograms of SPCE, MoS₂-SPCE, PANI-SPCE, and MoS₂-PANI/SPCE electrodes in the redox couple [Fe(CN)₆]^{3-/4-} with the potential window from -0.2 to 0.7 V at various scan rates are presented in **Figure 5**. A pair of distinct redox peaks are clearly seen for all the electrodes in Figure 5a-d. The minimum oxidation current response is observed for bare SPCE whereas the maximum oxidation current occurs in the case of the MoS₂-PANI/SPCE sample. The highest electrical conductiv-

ity of MoS₂-PANI/SPCE can facilitate the fastest electron transfer of [Fe(CN)₆]^{3-/4-}.

ECSA was also calculated for all the samples from the Randles-Sevcik equation^[62]:

$$i_p = 2.69 \times 10^5 n^{3/2} AD^{1/2} C\nu^{1/2} \quad (1)$$

where i_p is the peak current in amperes, A is the ECSA in mm², D is the diffusion coefficient in cm² s⁻¹, C is the concentration of

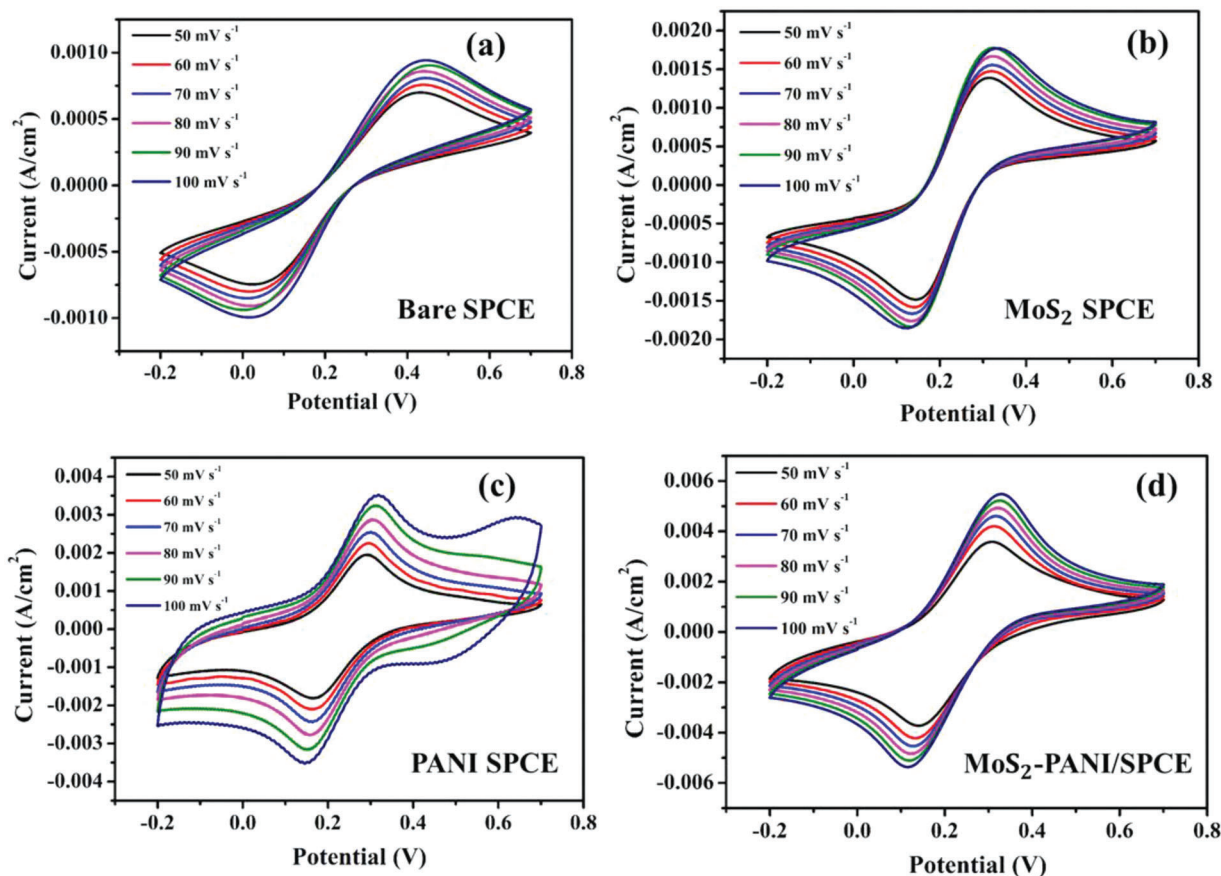


Figure 5. Cyclic voltammetry (CV) performance analysis of a) bare screen-printed carbon electrode (SPCE), b) MoS₂-SPCE, c) PANI-SPCE, d) MoS₂-PANI/SPCE in 5.0×10^{-3} M [Fe(CN)₆]^{3-/4-} containing 0.1 M KCl at different scan rates.

supporting electrolyte in M, n is the number of electrons involved in the redox reaction, and ν is the scan rate in V s^{-1} .

The anodic peak currents (i_{pa}) are plotted against the square root of the scan rate ($\nu^{1/2}$) and are shown in **Figure 6a–d**. The slope of i_p versus $\nu^{1/2}$ for all samples is evaluated as 0.006, 0.01, 0.037, and 0.05 $\text{mA mV}^{-1/2} \text{s}^{1/2}$, respectively. The diffusion coefficient of 5.0×10^{-3} M Fe(CN)₆^{4-/3-} solution containing 0.1 M KCl is $7.2 \times 10^{-6} \text{ cm}^2 \text{ s}^{-1}$ ^[63] and $n = 1$ for the redox couple. The maximum ECSA value (69.43 mm^2) is obtained for MoS₂-PANI/SPCE electrode by using the above equation and bare SPCE exhibited the least ECSA (8.33 mm^2). The active surface area of MoS₂ and PANI-modified SPCE are 13.88 and 41.66 mm^2 , respectively. The enhanced ECSA provides a more accessible area for an electrolyte which allows superior ion-to-electron transduction.

The impedance spectra of all four samples were recorded and the Nyquist plot is represented in **Figure 7** and **Figure S9** (Supporting Information). A model equivalent circuit was also employed to fit the impedance spectra of all four samples. The fitting of the MoS₂-PANI/SPCE composite is plotted in **Figure 7**. The equivalent circuit is also represented in the inset of **Figure 7**.

The first component of the equivalent circuit, R_1 takes care of the contact and the solution resistance. The parallel combination of a constant phase element (CPE) (Q_1) and a resistance (R_2) construct the second component of the equivalent circuit and indicates the existence of an interfacial layer. The resistance R_2 takes

interfacial and leakage resistance into account whereas, the mass capacitance can be expressed by the first CPE.

The CPE arises because of the inhomogeneity and nonlinearity in the electrode–electrolyte assembly and can be written as:

$$Z = Y_0(j\omega)^{-\alpha} \quad (2)$$

where the exponent of CPE is denoted by α and ω is the angular frequency. For $\alpha = 0$ the component is purely resistive and for $\alpha = 1$, it is purely capacitive.

The third component consisting of two modified Randles circuits signifies the charge transfer layer of the system. Where the presence of two modified Randles circuits signifies the presence of two different materials (PANI and MoS₂). The impedance spectra of all the other electrodes are also fitted using another model equivalent circuit and all the fitted plots and subsequent equivalent circuits are represented in **Figure S9** (Supporting Information). The absence of a second element of the modified Randles circuit confirms the absence of the second component for the bare SPCE, PANI-SPCE, and MoS₂-SPCE samples.

All the fitted parameters are further tabulated in **Table 1** and **Table S1** (Supporting Information). From **Table S1** (Supporting Information), it is found that the charge transfer resistance is maximum from the bare SPCE and minimum for the PANI electrode, signifying the higher conductivity of PANI. The charge

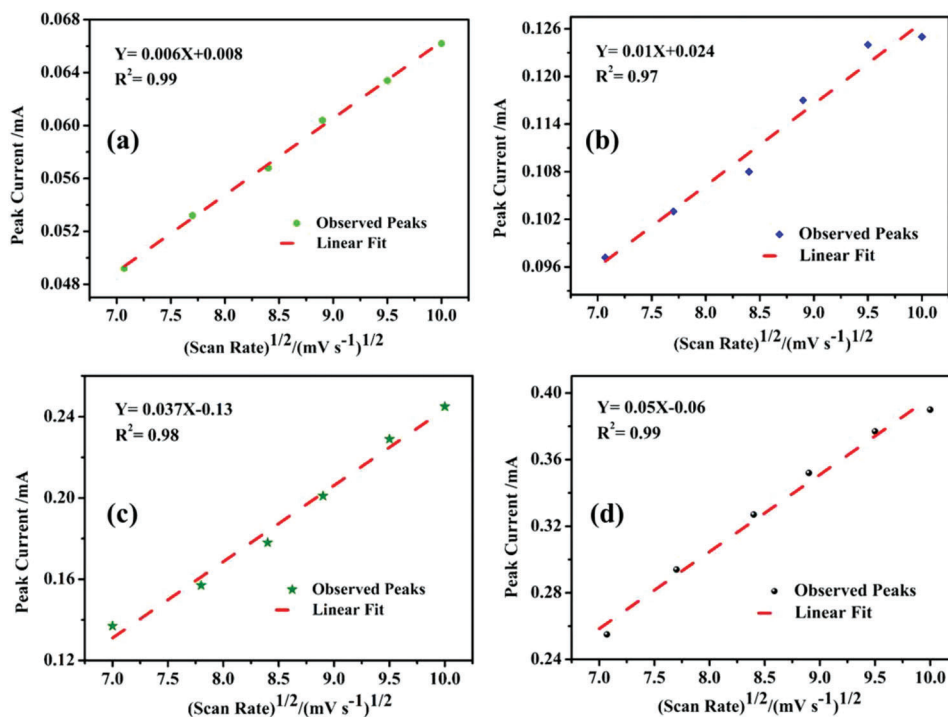


Figure 6. Randles–Sevcik plot shows the dependency of anodic peak current on the square root of scan rate for a) bare, b) MoS₂, c) PANI, and d) MoS₂-PANI/SPCE electrodes.

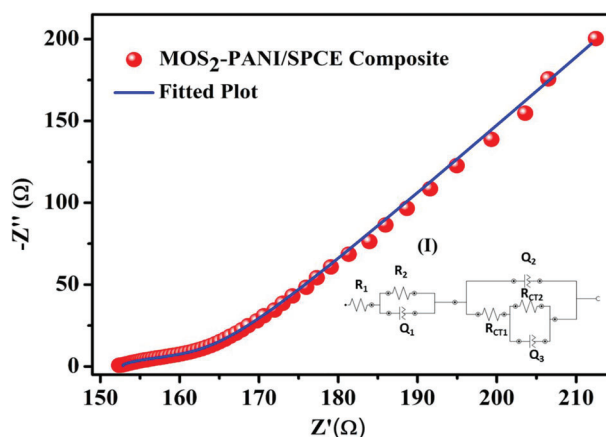


Figure 7. Experimental and fitted impedance spectra of MoS₂-PANI/SPCE composite and inset (I) shows the equivalent electrical circuit model.

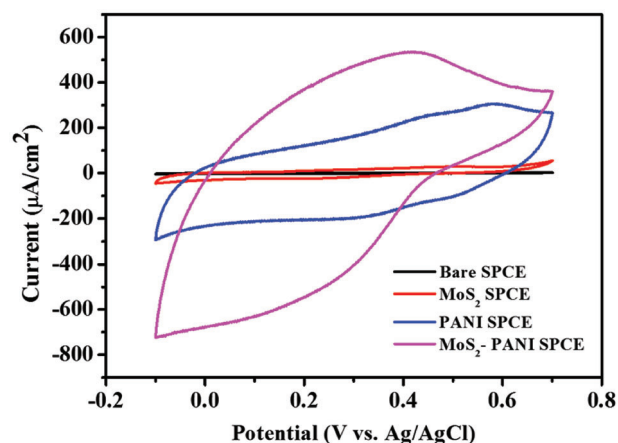


Figure 8. Cyclic voltammograms of all the electrodes in 1 M Na₂SO₄ (aqueous) electrolyte at constant scan rate of $\nu = 50 \text{ mV s}^{-1}$.

transfer resistance is intermediate for the MoS₂-modified electrode. From Table 1, it is quite evident that the charge transfer resistance is minimal for the composite electrodes which sig-

nifies better electron transfer kinetics and higher conductivity. Conductivity for each of the samples was calculated from the EIS measurement (Table S2, Supporting Information). For, MoS₂-

Table 1. The calculated values of electrochemical impedance spectroscopy (EIS) parameters through the fitting of experimental impedance spectra are based on the proposed equivalent circuit in Figure 5.

Sample	R_1 [Ω]	R_2 [Ω]	Q_1	Q_2	R_3 [Ω]	Q_3	R_4 [Ω]
MoS ₂ -PANI/SPCE composite	152	21.5	2.26 mHho $n = 0.97$	3.79 mHho $n = 0.94$	5.81	8.47 μ Hho $n = 0.555$	153

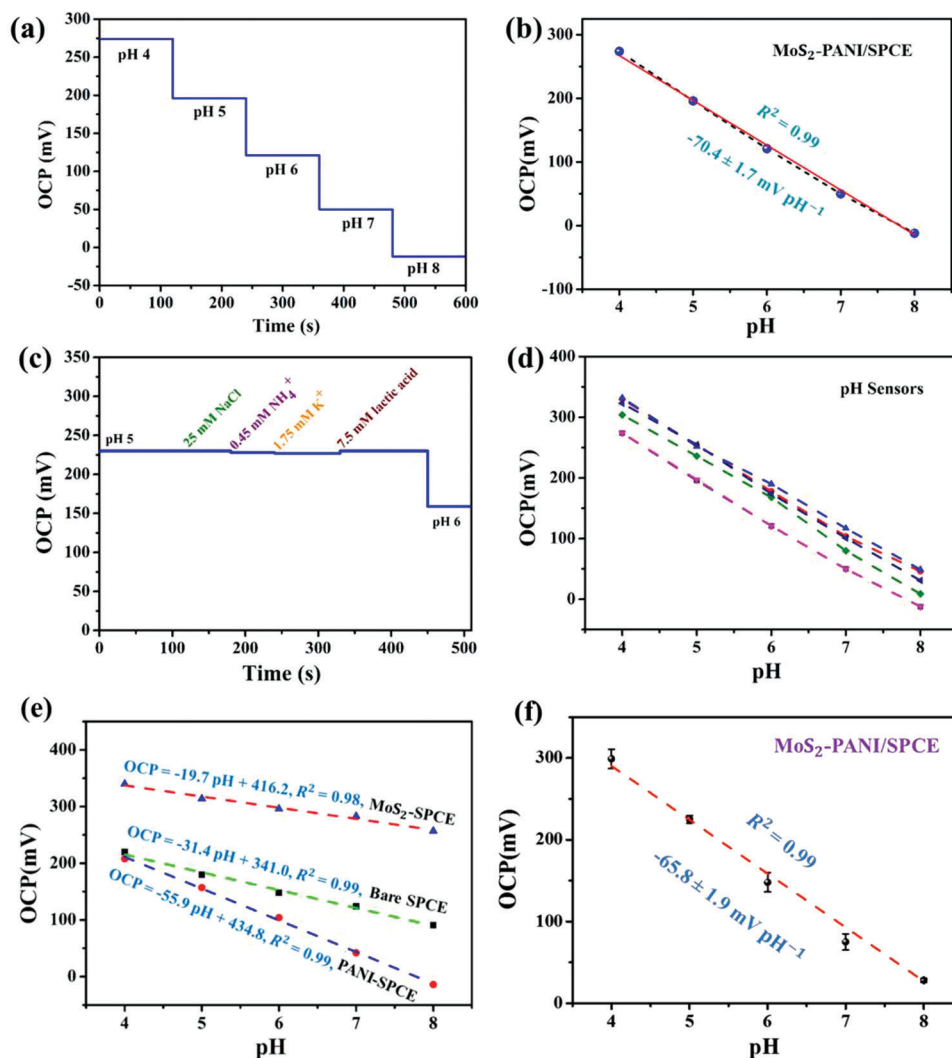


Figure 9. a) Open-circuit potential (OCP) versus time curve for buffer solutions with different pH from 4 to 8, b) calibration plot of the pH sensor ($\text{MoS}_2\text{-PANI/SPCE}$), c) selectivity test of pH sensor, d) reproducibility of pH sensors, e) calibration plot showing the sensitivity of bare SPCE and PANI SPCE based pH sensors. f) Response of sensor in presence of artificial sweat with different pH.

PANI/SPCE the conductivity is $4 \times 10^{-6} \text{ S m}^{-1}$ whereas for bare SPCE and $\text{MoS}_2\text{-SPCE}$ the estimated values are 1.28×10^{-7} and $1.02 \times 10^{-6} \text{ S m}^{-1}$. Thus, quantitatively, it is observed that there is a significant enhancement in the electrical conductivity.

The reduction of charge transfer resistance with respect to the pristine PANI sample indicates a synergistic effect between the PANI and the MoS_2 which not only enhances the charge transfer pathway but also increases the overall conductivity of the electrode.

To evaluate the electrochemical capacitive behavior of all the electrodes, the CV measurements were conducted (Figure 8) in $1 \text{ M Na}_2\text{SO}_4$ aqueous solution at a scan rate of 50 mV s^{-1} within the potential window from -0.1 to $+0.7 \text{ V}$ (versus Ag/AgCl). The CV curves show a quasi-rectangular structure indicating EDLC type behavior for all the electrodes. A significant increase in current and integrated area is observed for $\text{MoS}_2\text{-PANI/SPCE}$ electrode as compared to other electrodes. The areal-specific capaci-

ties were calculated from the enclosed area under the CV loops according to the following equation:^[64]

$$C = \frac{\oint I(V)dV}{2 A \times \nu \times \Delta V} \quad (3)$$

where C is the areal specific capacitance (mF cm^{-2}), $\oint I dV$ is the total current of the enclosed CV loop, A is the geometrical electrode area of the electrode in cm^2 , ν is the scan rate (mV s^{-1}), and ΔV is the scanned potential window (V).

The specific areal capacitance value for $\text{MoS}_2\text{-PANI/SPCE}$ is found to be 7.5 mF cm^{-2} whereas, for bare, MoS_2 and PANI-SPCE electrodes the estimated values were 0.2 , 0.3 , and 3.4 mF cm^{-2} , respectively. Higher specific capacitance can be attributed to the fast ionic diffusion process at the electrode-electrolyte interface. On the other hand, lower areal capacitance implies the poor electrical conductivity of electrodes.

Table 2. Comparison of different pH sensors in terms of pH range, response time, and sensitivity.

Material	pH range	Response time	Sensitivity [mV pH ⁻¹]	Reference
WO ₃ nanoparticles	5–9	23–28 s	56.7 ± 1.3	[70]
Polyaniline nanofibers	3.9–10.1	12.8 s	62.4	[71]
Niobium	2–12	12.5 min	41	[72]
SWCNTs	3–11	–	59.7 ± 1.5	[73]
ZnO	1–9	–	59	[74]
RuO _x nanorods	2–10	2 s	58.05	[75]
IrO ₂	4–8	–	47.54	[76]
PANI/PP/LIG	4–7	–	75.06	[77]
PANI-CNT	4–8	–	71.44	[1]
PANI	3–8	<30s	59.6	[78]
LIG-PANI	4–9.5	3–4 min	45	[79]
TA-RGO	1–10	–	53.0 ± 0.7	[80]
F–Ti ₃ C ₂ T _x /PANI	1–11	–	41.91	[81]
MoS ₂ -PANI/SPCE	4–8	2–3 min	70.4 ± 1.7	This work

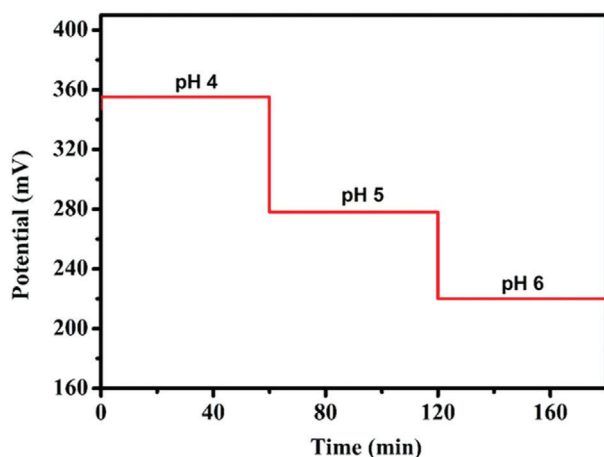


Figure 10. The stability test indicates a linear relationship between open circuit potential (OCP) and pH.

3.3. Electrochemical Investigation of the Fabricated pH Sensor

Figure 9 illustrates the electrochemical performances of PANI-modified MoS₂-SPCE pH sensor under ambient conditions. H⁺ selective PANI deposition was carried out by electropolymerization onto a MoS₂ drop-casted carbon electrode. The sensing performance was monitored by measuring the OCP value with the variation in pH of standard buffer solutions ranging from 4 to 8. The OCP measurements were carried out in a two-electrode system, where both the working electrodes and commercial Ag/AgCl (3 M KCl) reference electrode were dipped in different pH solutions. Figure 9a depicts the OCP values versus time and 9b is used to produce the linear calibration curves. This sensor yielded a linear behavior in the pH range 4 to 8 with an excellent sensitivity of 70.4 ± 1.7 mV pH⁻¹, and high regression coefficient ($R^2 = 0.99$) as evident from Figure 9b. The sensitivity was calculated from the slope of the calibration curve which exceeded the Nernst limit of pH sensitivity. The sensitivity and

conductivity of the PANI-based pH sensors are reported to be dependent upon the crystalline and amorphous phases of PANI and the manufacturing method.^[28,65,66] Therefore, the high sensitivity and surpass of the Nernst limit of the MoS₂-PANI/SPCE-based pH sensor in our investigation seems to be originated from the effective polymerization of aniline on the MoS₂-SPCE electrode. The dependence of OCP E of an ISE with the pH values in the test solution is strongly correlated with Nernst's equation:^[67]

$$E = E^0 - \left(\frac{2.303 RT}{nF} \right) pH \quad (4)$$

where, E^0 is the standard redox potential, “ R ” is the universal gas constant, “ T ” is the absolute temperature, “ n ” is the number of electrons involved in the electrochemical reaction, and “ F ” is Faraday's constant.

Figure 9c shows the selectivity results of the potentiometric pH sensor indicating the ability to discriminate and measure the target H⁺ ions in presence of other interfering ions. The potentiometric selectivity test of pH sensor was performed by subsequently adding other ions which include Na⁺, Cl⁻, NH₄⁺, K⁺, and lactic acid and OCP values were recorded accordingly.^[27,68] However, evidently, there were no significant changes in OCP values to the added interfering ions except for H⁺ ions because of its detection by deprotonation technique on the PANI-modified electrode. This shows that the sensor is selectively responsive to H⁺ ions and hence makes it feasible for pH analysis in human sweat. Furthermore, reproducibility is one of the most important factors in potentiometric pH sensors, consistent analysis of which can be achieved from the individual sensor. The reproducibility of six sensors is reported in Figure 9d. In Figure 9e, we have shown the performance of neat PANI, bare, and MoS₂ SPCE as sensitive working electrodes for the detection of pH in the 4 to 8. The OCP of both electrodes exhibited a corresponding decrease, followed by increased pH values. For PANI-SPCE the obtained calibration plot displays a sub-Nernstian behavior with a slope of 55.9 mV pH⁻¹ and both bare and MoS₂ SPCE show inferior

responses with a slope of 31.4 and 19.7 mV pH⁻¹ in comparison with the MoS₂-PANI/SPCE electrode.

We have also investigated the feasibility of the biosensors which was achieved by assessing their performance in artificial sweat solutions. Figure 9f demonstrates the characterization result of a fabricated MoS₂-PANI/SPCE-based pH sensor in the artificial sweat solution. Artificial sweat solution was prepared according to the European reference method EN1811:2011^[69] by mixing urea (0.1 wt%), and lactic acid (0.1 wt%) in deionized water with varying pH from 4 to 8. The sensitivity of the pH sensor was found to be 65.8 ± 1.9 mV pH⁻¹ with high regression coefficient (0.99). Many materials have been used for the fabrication of wearable and flexible electrochemical pH sensors. Table 2 summarizes the performance of various materials used for fabricating pH sensors.

The long-term stability test of the proposed pH sensor is captured in Figure 10. The result in Figure 10 indicates that the fabricated pH sensor was almost stable for different pH electrolytes ranging from 4 to 6 over a 180 min of continuous measurement. For the flexibility test of the fabricated sweat pH sensor, different bending angles were applied to the sensor to evaluate the OCP value changes during the detection process. As shown in Figure S10 (Supporting Information), the sensor was bent first at different bending angles and then the OCP value was recorded after unbending in the standard PBS with pH 6. From the graph it is clear that the OCP value was almost stable at the different bending deformations. The measurements for the sensor in each case (bent and after unbending) were allowed to continue for 180–200 s to reach a steady state.

Our study indicates that the high sensitivity, repeatability, reproducibility, and practicability of the electrode can be used as a noninvasive and wearable system for continuous, real-time personal healthcare monitoring.

Overall, the current study reveals that PANI functionalized MoS₂-SPCE electrodes can serve as flexible potentiometric pH sensing platforms and other analytes in human perspiration.

4. Conclusion

Accurate and continuous monitoring of pH in human biofluids is important for disease diagnosis and treatment. Herein, we have presented the development of a stable, flexible, and highly sensitive electrochemical sensing platform for the detection of pH in sweat. The pH sensors were completely fabricated via electrodeposition of PANI on MoS₂ nanosheets drop-coated flexible SPCE substrates. The biosensor exhibited high sensitivity of 70.4 ± 1.7 mV pH⁻¹ with a linear super-Nernstian response. In addition, the sensor showed high selectivity without any interference from ions and metabolites that can exist in human sweat. Fast response time, repeatability, and reproducibility were also observed for the sensor. This work manifests the high potential application of our fabricated sensor for continuous and real-time monitoring of various physiological components in human sweat including pH. Furthermore, our proposed flexible pH sensor can be integrated into a miniaturized skin-attachable and non-invasive device for clinical diagnostics.

Supporting Information

Supporting Information is available from the Wiley Online Library or from the author.

Acknowledgements

S.C. and D.D. are indebted to Shiv Nadar Institute of Eminence for providing Ph.D. scholarships.

Conflict of Interest

The authors declare no competing financial interests.

Data Availability Statement

Data sharing is not applicable to this article as no new data were created or analyzed in this study.

Keywords

artificial sweat, electrochemical biosensors, pH sensors, screen printed carbon electrodes, wearable sensors

Received: January 9, 2023

Revised: April 4, 2023

Published online:

- [1] S. Y. Oh, S. Y. Hong, Y. R. Jeong, J. Yun, H. Park, S. W. Jin, G. Lee, J. H. Oh, H. Lee, S.-S. Lee, J. S. Ha, *ACS Appl. Mater. Interfaces* **2018**, *10*, 13729.
- [2] L. Manjakkal, S. Dervin, R. Dahiya, *RSC Adv.* **2020**, *10*, 8594.
- [3] A. J. Bandodkar, J. Wang, *Trends Biotechnol.* **2014**, *32*, 363.
- [4] A. Ganguly, S. Prasad, *Sensors* **2019**, *19*, 4590.
- [5] T. Kaya, G. Liu, J. Ho, K. Yelamarthi, K. Miller, J. Edwards, A. Stannard, *Electroanalysis* **2019**, *31*, 411.
- [6] J. Kim, A. S. Campbell, B. E.-F. De Ávila, J. Wang, *Nat. Biotechnol.* **2019**, *37*, 389.
- [7] I. Seymour, B. O'sullivan, P. Lovera, J. F. Rohan, A. O'riordan, *Sens. Actuators, B* **2020**, *325*, 128774.
- [8] A. J. C. Wahl, I. P. Seymour, M. Moore, P. Lovera, A. O'riordan, J. F. Rohan, *Electrochim. Acta* **2018**, *277*, 235.
- [9] P. Pirovano, M. Dorrian, A. Shinde, A. Donohoe, A. J. Brady, N. M. Moyna, G. Wallace, D. Diamond, M. McCaul, *Talanta* **2020**, *219*, 121145.
- [10] S. Choudhury, S. Roy, G. Bhattacharya, S. Fishlock, S. Deshmukh, S. Bhowmick, J. McLaughlin, S. S. Roy, *Electrochim. Acta* **2021**, *387*, 138341.
- [11] S. Robinson, A. H. Robinson, *Physiological reviews* **1954**, *34*, 202.
- [12] Q. Zhai, L. W. Yap, R. Wang, S. Gong, Z. Guo, Y. Liu, Q. Lyu, J. Wang, G. P. Simon, W. Cheng, *Anal. Chem.* **2020**, *92*, 4647.
- [13] B. U. W. Lei, T. W. Prow, *Biomed. Microdevices* **2019**, *21*, 81.
- [14] J. Zhao, Y. Lin, J. Wu, H. Y. Y. Nyein, M. Bariya, L. C. Tai, M. Chao, W. Ji, G. Zhang, Z. Fan, A. Javey, *ACS Sens.* **2019**, *4*, 1925.
- [15] R. Wang, Q. Zhai, Y. Zhao, T. An, S. Gong, Z. Guo, Q. Shi, Z. Yong, W. Cheng, *J. Mater. Chem. B* **2020**, *8*, 3655.
- [16] V. P. Kutyschenko, M. Molchanov, P. Beskaravayny, V. N. Uversky, M. A. Timchenko, *PLoS One* **2011**, *6*, e28824.
- [17] V. C. Diculescu, M. Beregoi, A. Evangelidis, R. F. Negrea, N. G. Apostol, I. Enculescu, *Sci. Rep.* **2019**, *9*, 8902.

- [18] A. Amodio, A. F. Adedeji, M. Castronovo, E. Franco, F. Ricci, *J. Am. Chem. Soc.* **2016**, *138*, 12735.
- [19] M. Bariya, H. Y. Y. Nyein, A. Javey, *Nat. Electron.* **2018**, *1*, 160.
- [20] M. T. Ghoneim, A. Nguyen, N. Dereje, J. Huang, G. C. Moore, P. J. Murzynowski, C. Dagdeviren, *Chem. Rev.* **2019**, *119*, 5248.
- [21] J. H. Yoon, S.-M. Kim, H. J. Park, Y. K. Kim, D. X. Oh, H.-W. Cho, K. G. Lee, S. Y. Hwang, J. Park, B. G. Choi, *Biosens. Bioelectron.* **2020**, *150*, 111946.
- [22] N. M. Maalouf, M. A. Cameron, O. W. Moe, K. Sakhaee, *Clin. J. Am. Soc. Nephrol.* **2010**, *5*, 1277.
- [23] Z. Sonner, E. Wilder, J. Heikenfeld, G. Kasting, F. Beyette, D. Swaile, F. Sherman, J. Joyce, J. Hagen, N. Kelley-Loughnane, R. Naik, *Biomecrofluidics* **2015**, *9*, 031301.
- [24] W. Dang, L. Manjakkal, W. T. Navaraj, L. Lorenzelli, V. Vinciguerra, R. Dahiya, *Biosens. Bioelectron.* **2018**, *107*, 192.
- [25] W. Nikolajek, H. Emrich, *Klin. Wochenschr.* **1976**, *54*, 287.
- [26] H. Y. Y. Nyein, W. Gao, Z. Shahpar, S. Emaminejad, S. Challa, K. Chen, H. M. Fahad, L. C. Tai, H. Ota, R. W. Davis, A. Javey, *ACS Nano* **2016**, *10*, 7216.
- [27] M. J. Patterson, S. D. R. Galloway, M. A. Nimmo, *Exp. Physiol.* **2000**, *85*, 869.
- [28] A. J. Bandodkar, V. W. S. Hung, W. Jia, G. Valdés-Ramírez, J. R. Windmiller, A. G. Martínez, J. Ramírez, G. Chan, K. Kerman, J. Wang, *Analyst* **2013**, *138*, 123.
- [29] T. R. Dargaville, B. L. Farrugia, J. A. Broadbent, S. Pace, Z. Upton, N. H. Voelcker, *Biosens. Bioelectron.* **2013**, *41*, 30.
- [30] L. Manjakkal, D. Szwagierczak, R. Dahiya, *Prog. Mater. Sci.* **2020**, *109*, 100635.
- [31] Y. Tang, S. Gan, L. Zhong, Z. Sun, L. Xu, C. Liao, K. Lin, X. Cui, D. He, Y. Ma, W. Wang, L. Niu, *Adv. Funct. Mater.* **2022**, *32*, 2107653.
- [32] H. Y. Y. Nyein, L.-C. Tai, Q. P. Ngo, M. Chao, G. B. Zhang, W. Gao, M. Bariya, J. Bullock, H. Kim, H. M. Fahad, A. Javey, *ACS Sens.* **2018**, *3*, 944.
- [33] W. S. Lee, Y. Park, Y. Cho, *ACS Applied Materials and Interfaces* **2014**, *6*, 12189.
- [34] Y. Qin, H. J. Kwon, M. M. R. Howlader, M. J. Deen, *RSC Adv.* **2015**, *5*, 69086.
- [35] E. Bakker, P. Bühlmann, E. Pretsch, *Chem. Rev.* **1997**, *97*, 3083.
- [36] A. U. Alam, Y. Qin, S. Nambiar, J. T. W. Yeow, M. M. R. Howlader, N.-X. Hu, M. J. Deen, *Prog. Mater. Sci.* **2018**, *96*, 174.
- [37] A. Talaie, *Polymer* **1997**, *38*, 1145.
- [38] L. Ren, G. Zhang, Z. Yan, L. Kang, H. Xu, F. Shi, Z. Lei, Z.-H. Liu, *ACS Appl. Mater. Interfaces* **2015**, *7*, 28294.
- [39] Y. Wang, X. Lv, S. Zou, X. Lin, Y. Ni, *RSC Adv.* **2021**, *11*, 10941.
- [40] M. S. Raghu, K. Y. Kumar, S. Rao, T. Aravinda, B. P. Prasanna, M. K. Prashanth, *Polym. Bull.* **2018**, *75*, 4359.
- [41] N. Dalila R, M. K. Md Arshad, S. C. B. Gopinath, W. M. W. Norhaimi, M. F. M. Fathil, *Biosens. Bioelectron.* **2019**, *132*, 248.
- [42] S. Barua, H. S. Dutta, S. Gogoi, R. Devi, R. Khan, *ACS Appl. Nano Mater.* **2018**, *1*, 2.
- [43] K. Kalantar-Zadeh, J. Z. Ou, *ACS Sens.* **2016**, *1*, 5.
- [44] K.-J. Huang, J.-Z. Zhang, Y.-J. Liu, L.-L. Wang, *Sens. Actuators, B* **2014**, *194*, 303.
- [45] T. Yang, H. Chen, T. Ge, J. Wang, W. Li, K. Jiao, *Talanta* **2015**, *144*, 1324.
- [46] B. Rajagopalan, S. H. Hur, J. S. Chung, *Nanoscale Res. Lett.* **2015**, *10*, 183.
- [47] D. Sahoo, B. Kumar, J. Sinha, S. Ghosh, S. S. Roy, B. Kaviraj, *Sci. Rep.* **2020**, *10*, 10759.
- [48] N. Maity, A. Mandal, A. K. Nandi, *J. Mater. Chem. C* **2017**, *5*, 12121.
- [49] K. Sudhakara Prasad, G. Muthuraman, J.-M. Zen, *Electrochem. Commun.* **2008**, *10*, 559.
- [50] S. Dutta, A. Dutta Chowdhury, S. Biswas, E. Y. Park, N. Agnihotri, A. De, S. De, *Biochem. Eng. J.* **2018**, *140*, 130.
- [51] S. Saha, N. Chaudhary, H. Mittal, G. Gupta, M. Khanuja, *Int. Nano Lett.* **2019**, *9*, 127.
- [52] T. V. Freitas, E. A. Sousa, G. C. Fuzari Jr, E. P. S. Arlindo, *Mater. Lett.* **2018**, *224*, 42.
- [53] M. S. Nam, U. Patil, B. Park, H. B. Sim, S. C. Jun, *RSC Adv.* **2016**, *6*, 101592.
- [54] J. Jayapriya, J. Gopal, V. Ramamurthy, U. Kamachi Mudali, B. Raj, *Composites, Part B* **2012**, *43*, 1329.
- [55] M. Vasudevan, M. J. Y. Tai, V. Perumal, S. C. B. Gopinath, S. S. Murthe, M. Ovinis, N. M. Mohamed, N. Joshi, *Biotechnol. Appl. Biochem.* **2021**, *68*, 1386.
- [56] Q. Lin, X. Dong, Y. Wang, N. Zheng, Y. Zhao, W. Xu, T. Ding, *J. Mater. Sci.* **2020**, *55*, 6637.
- [57] Y.-L. Bai, Y.-S. Liu, C. Ma, K.-X. Wang, J.-S. Chen, *ACS Nano* **2018**, *12*, 11503.
- [58] Z. Zhang, H. Zhao, Y. Teng, X. Chang, Q. Xia, Z. Li, J. Fang, Z. Du, K. Świerczek, *Adv. Energy Mater.* **2018**, *8*, 1700174.
- [59] X. Li, C. Zhang, S. Xin, Z. Yang, Y. Li, D. Zhang, P. Yao, *ACS Appl. Mater. Interfaces* **2016**, *8*, 21373.
- [60] H. Liu, H. Hu, J. Wang, P. Niehoff, X. He, E. Paillard, D. Eder, M. Winter, J. Li, *ChemElectroChem* **2016**, *3*, 922.
- [61] I.-W. P. Chen, Y.-C. Chou, P.-Y. Wang, *J. Phys. Chem. C* **2019**, *123*, 17864.
- [62] R. Ganatra, Q. Zhang, *ACS Nano* **2014**, *8*, 4074.
- [63] M. Thakurathi, E. Gurung, M. M. Cetin, V. D. Thalangamaarachchige, M. F. Mayer, C. Korzeniewski, E. L. Quitevis, *Electrochim. Acta* **2018**, *259*, 245.
- [64] Z. O. Ameur, M. M. Husein, *Sep. Sci. Technol.* **2013**, *48*, 681.
- [65] D. Banerjee, K. J. Sankaran, S. Deshmukh, M. Ficek, G. Bhattacharya, J. Ryl, D. M. Phase, M. Gupta, R. Bogdanowicz, I. N. Lin, A. Kanjilal, K. Haenen, S. S. Roy, *J. Phys. Chem. C* **2019**, *123*, 15458.
- [66] S. Bause, M. Decker, F. Gerlach, J. Näther, F. Köster, P. Neubauer, W. Vonau, *J. Solid State Electrochem.* **2018**, *22*, 51.
- [67] L. Abell, P. N. Adams, A. P. Monkman, *Polymer* **1996**, *37*, 5927.
- [68] F. Mazzara, B. Patella, C. D'agostino, M. G. Bruno, S. Carbone, F. Lopresti, G. Aiello, C. Torino, A. Vilasi, A. O'riordan, R. Inguanta, *Chemosensors* **2021**, *9*, 169.
- [69] L. B. Baker, *Temperature* **2019**, *6*, 211.
- [70] L. Santos, J. P. Neto, A. Crespo, D. Nunes, N. Costa, I. M. Fonseca, P. Barquinha, L. Pereira, J. Silva, R. Martins, E. Fortunato, *ACS Appl. Mater. Interfaces* **2014**, *6*, 12226.
- [71] H. J. Park, J. H. Yoon, K. G. Lee, B. G. Choi, *Nano Convergence* **2019**, *6*, 9.
- [72] T. D. Singewald, I. Traxler, G. Schimo-Aichhorn, S. Hild, M. Valtiner, *Sens. Bio-Sens. Res.* **2022**, *35*, 100478.
- [73] C. A. Li, K. N. Han, X. H. Pham, G. H. Seong, *Analyst* **2014**, *139*, 2011.
- [74] L. Maiolo, S. Mirabella, F. Maita, A. Alberti, A. Minotti, V. Strano, A. Pecora, Y. Shacham-Diamand, G. Fortunato, *Appl. Phys. Lett.* **2014**, *105*, 093501.
- [75] E. Tanumihardja, W. Olthuis, A. van den Berg, *Sensors* **2018**, *18*, 2901.
- [76] M. L. Zamora, J. M. Dominguez, R. M. Trujillo, C. B. Goy, M. A. Sánchez, R. E. Madrid, *Sens. Actuators, B* **2018**, *260*, 601.
- [77] M. A. Zahed, S. C. Barman, P. S. Das, M. Sharifuzzaman, H. S. Yoon, S. H. Yoon, J. Y. Park, *Biosens. Bioelectron.* **2020**, *160*, 112220.
- [78] P. Mostafalu, M. Akbari, K. A. Alberti, Q. Xu, A. Khademhosseini, S. R. Sonkusale, *Microsyst. Nanoeng.* **2016**, *2*, 16039.
- [79] M. Jose, S. K. Mylavarapu, S. K. Bikkarolla, J. Machiels, K. J. Sankaran, J. McLaughlin, A. Hardy, R. Thoenen, W. Deferme, *Adv. Eng. Mater.* **2022**, *24*, 2101087.
- [80] K. Lin, J. Xie, Y. Bao, Y. Ma, L. Chen, H. Wang, L. Xu, Y. Tang, Z. Liu, Z. Sun, S. Gan, L. Niu, *Electrochem. Commun.* **2022**, *137*, 107261.
- [81] L. Chen, F. Chen, G. Liu, H. Lin, Y. Bao, D. Han, W. Wang, Y. Ma, B. Zhang, L. Niu, *Anal. Chem.* **2022**, *94*, 7319.